TÜBİTAK

Turkish Journal of Physics

http://journals.tubitak.gov.tr/physics/

Research Article

Turk J Phys
(2018) 42: 501 – 508
© TÜBİTAK
doi:10.3906/fiz-1711-24

Broadband spectral splitting of white light via 2D diffractive optical elements

Yalın BAŞAY[1,2], **Emre YÜCE**[1,2,*]

[1]Programmable Photonics Group, Department of Physics, Middle East Technical University, Ankara, Turkey
[2]Center for Solar Energy and Applications (GÜNAM), Middle East Technical University, Ankara, Turkey

Received: 04.12.2017 • **Accepted/Published Online:** 03.09.2018 • **Final Version:** 12.10.2018

Abstract: An effective way of increasing the efficiency of solar cells is to spectrally split sunlight into several frequencies and absorb each frequency using appropriate photovoltaic materials. In this study, we establish a method to show spectral splitting of broadband solar light via iteratively optimized diffractive optical elements. We develop an algorithm in order to calculate 2D holographic patterns that focus two different frequencies to designated positions.

Key words: Spectral splitting, diffraction, solar cells

1. Introduction

The energy need of people increases continuously and the obligation to develop more efficient energy sources is a contemporary challenge. Sustainable and nature-friendly energy sources must come into prominence for humanity to continue its existence. Given the tremendous amount of solar radiation reaching the earth's surface each day, solar energy is one of the most promising energy sources. However, most of the solar energy reaching a specific region cannot be converted into electricity. For single-junction solar cells, the theoretical efficiency limit is 33.5% [1]. Recently, 29.3% efficiency has been reported experimentally for a single-junction solar cell. The efficiency is reported to increase up to 46% by using multijunction solar panels with concentrators [2].

Multijunction solar cells provide better efficiency given their architecture that consists of different materials with peak efficiencies at different frequencies of light. The electronic band structure of semiconductor materials determines the bandwidth over which the material can absorb the solar energy. By stacking junctions of different materials in such a way that the highest energy photons are absorbed by the top layer and subsequent layers absorb lower energy photons, the efficiency is maximized. However, there are several disadvantages of this technique: i) the energy losses due to reflection at interfaces of mechanically stacked devices and ii) the complexity of fabrication via epitaxial growth process [3]. On the other hand, fabrication of laterally displaced junctions is simpler and these junctions provide similar efficiency as the vertically stacked junctions. However, the laterally displaced junctions require the incident white light to be spectrally split, which is a challenge for broadband solar light.

Remarkably, diffractive optical elements (DOEs), which consist of array of microstructures, provide the opportunity to control diffraction and thereby enable beam processing, imaging, and spectroscopy in large-scale areas [4–6]. DOEs are also applied to multijunction solar cells for spectrally splitting broadband solar light [3,7,8]. DOEs are generally designed in one dimension and optimized for obtaining increased spectral splitting

*Correspondence: eyuce@metu.edu.tr

This work is licensed under a Creative Commons Attribution 4.0 International License.

efficiency. On the other hand, the DOEs that are optimized in two dimensions can provide spectral splitting and solar concentration simultaneously.

Here, we design two-dimensional DOEs, which simultaneously split light into different frequencies as well as concentrating solar light. Our optimization technique enables the design of DOEs that direct solar light into predesignated positions at the same time, providing easy adaptation to different fabrication processes.

2. Theory and algorithm

Wave properties of light, especially interference and diffraction, make it possible to split white light into different frequencies. A desired intensity pattern can be obtained at a given position by gaining control on diffraction of light beams. As illustrated in Figure 1a, partitioning the plane into sufficiently small pieces (pixels) results in diffraction. The light, passing from each pixel, diverges and interferes at the output plane. The resultant interference pattern can be controlled by changing the refractive index of each pixel, leading to manipulation of phase differences between diffracted light beams. These phase changes lead to constructive and destructive interferences at different positions at the output plane. These positions at the output plane also depend on the frequency of light. As a result, two distinct frequencies interfere constructively and destructively at different positions at the output plane.

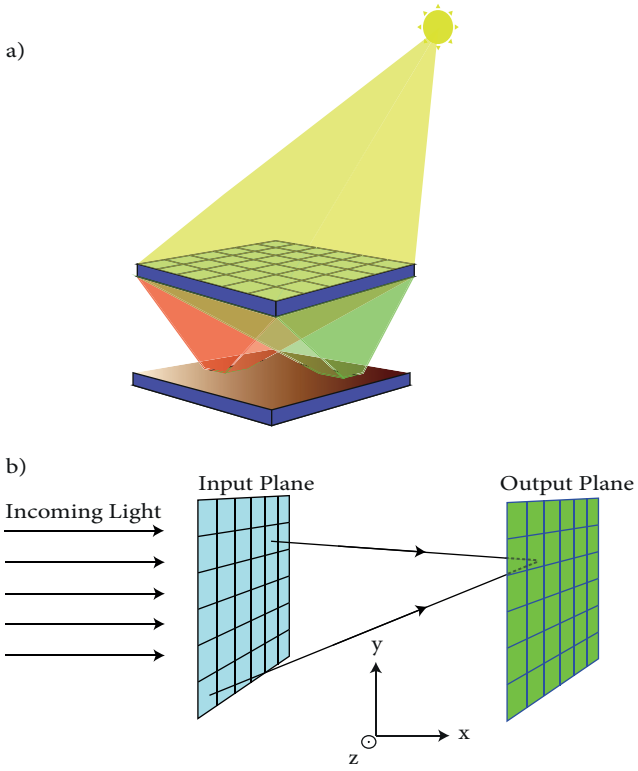

Figure 1. (a) Schematic representation of broadband spectral splitting. (b) The intensity pattern at the output plane is calculated by summing up the diffracted light from each pixel at input plane. The phase difference between the pixels is taken into account by the height profile of the pixels and the optical distance between input and output planes.

We use the method developed by Dong et al. [8] and divide both input and output planes into pixels as shown in Figure 1b. The resultant interference at the output plane is calculated by using the following equation:

$$U_{2m\alpha} = \sum_{k=1}^{N_1} G_{mk}\left(\lambda_\alpha\right) U_{1k}\left(\lambda_\alpha\right), \tag{1}$$

where $U_{2m\alpha}$ is the value of the wave function at the mth pixel of the output plane for the wavelength of λ_α, U_{1k} the value of the wave function at the kth pixel of the input plane, G_{mk} the kernel function that fulfills the relation between the kth pixel of input and mth pixel of output wave functions, and N_1 the total number of pixels [8]. Eq. (1) indicates that the effect of an input pixel on an output pixel is determined by two values: U_1, which contains the information of phase just after the input plane, and G, which includes the information of distance between input and output pixels. The equations for calculating these values in one-dimensional geometry are:

$$U_{1k}(\lambda_\alpha) = \rho_{1k} \exp\left[i2\pi h_{1k}\left(n_S - 1\right)/\lambda_\alpha\right], \tag{2}$$

$$G\left(y_2,\, y_1; l,\, \lambda_\alpha\right) = \left(\frac{1}{i\lambda_\alpha l}\right)^{1/2} \exp\left(i2\pi l/\lambda_\alpha\right) \times \exp\left(i\pi\left(y_2 - y_1\right)^2 \Big/ \lambda_\alpha l\right) \tag{3}$$

where ρ_{1k} is the amplitude and h_{1k} the depth value of the kth input pixel, n_S the refractive index of input material, l the distance between input and output planes, and y_1 and y_2 the positions of input and output pixels, respectively. The product of Eq. (2) and Eq. (3) gives the complete information about phases. Note that both the depth pattern and the refractive index pattern can be used since both change the optical path length. For two dimensions, we reformulate the transfer function G as:

$$G\left(y_2,\, y_1,\, z_2, z_1\,; l,\, \lambda_\alpha\right) = \left(\frac{1}{i\lambda_\alpha l}\right)^{1/2} \exp\left(i2\pi l/\lambda_\alpha\right) \times \exp\left(i\pi((y_2 - y_1)^2 + (z_2 - z_1)^2)/\lambda_\alpha l\right), \tag{4}$$

where z_1 and z_2 are the second position components of input and output pixels, respectively. For obtaining a complete pattern, effects of diffracted light beams from all input pixels must be summed up. Lastly, we calculate the intensity pattern from the field distribution using:

$$I(y_2,\ z_2;\, \lambda_\alpha) = \left| \sum_{k=1}^{N} G\left(y_2,\, y_1,\, z_2, z_1\,; l,\, \lambda_\alpha\right) \cdot U_{1k}(\lambda_\alpha) \right|^2. \tag{5}$$

This calculation is performed iteratively for finding the optimum depth or refractive index profile. Effective algorithms such as the Gerchberg–Saxton algorithm can be used for easing the computational load [9,10]. Our algorithm is based on Fourier optimization, which is performed by scanning pixels at the input plane one by one and calculating the resultant intensity pattern at the output plane. If intensity at a desired region increases, the algorithm accepts that input pattern and rejects it otherwise. By following these steps for more than one wavelength and introducing an "and" gate, we manage to focus each frequency to designated positions. As a result, both spectral splitting and concentration are achieved. Figure 2 illustrates a detailed diagram that shows each step of our algorithm.

3. Results

We run our optimization algorithm for a refractive index of n = 1.495 at the input plane for each pixel and we set the height profile range between 0 and 10 μm with a step size of 1 μm. The distance between planes is set to 0.4 m and we choose two wavelengths as 400 nm and 800 nm. For one dimension, the size of the DOE

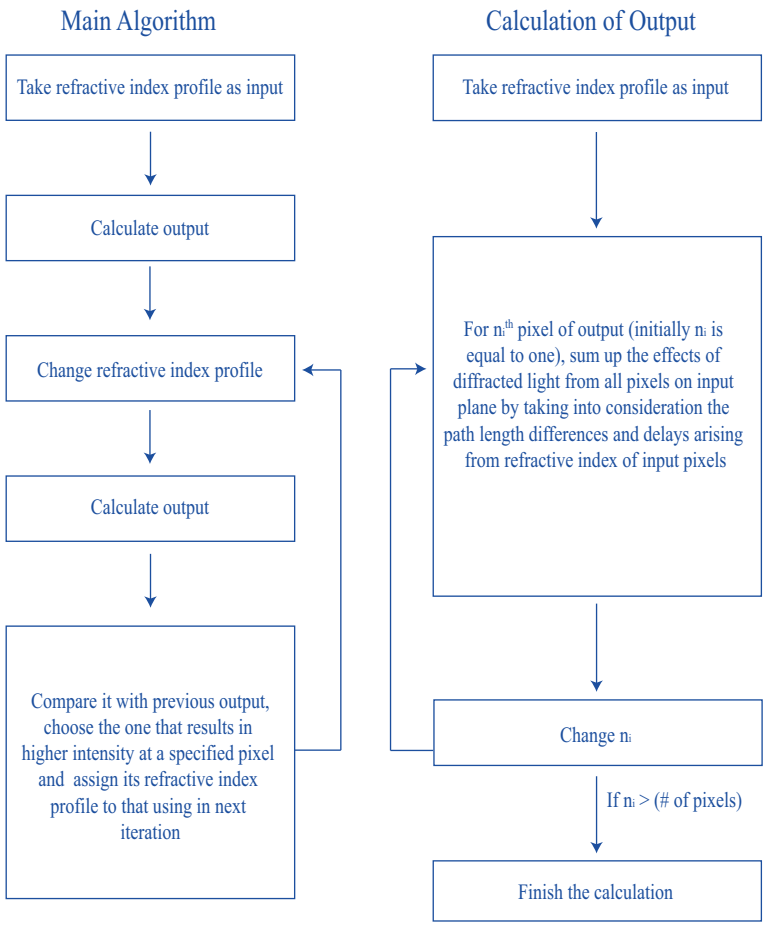

Figure 2. The schematic diagram of the optimization algorithm.

is set to 10 mm and the positions of points where the light will be focused are designed to be 2 mm for 400 nm and 8 mm for 800 nm. For 1D calculations, we optimize 1000 pixels. In the transverse plane the size of a pixel is set to 10 μm. After assigning these values to related variables, the algorithm creates a matrix, the size of which is 1000 $\times$ 1, and assigns one of the 11 equally spaced heights between 0 and 10 μm randomly to each element (with 1 μm step size) of this matrix. As a result, the initial height profile is generated. Then, for every single output pixel, the effect of diffracted beams from each input pixel is calculated. This calculation is performed for both 400 nm and 800 nm wavelengths. After that, the height of each input pixel is changed from 0 to 10 μm and the calculation is repeated iteratively. Then the obtained intensity value at the output plane is compared with the previous value. If both of the values for 400 nm and 800 nm increase, the height profile is accepted. The resultant height profile is shown in Figure 3a. A high resolution view of the height profile between 9 mm and 10 mm can be seen in Figure 3b. The resulting intensity pattern for light passing through the calculated height profile is shown in Figure 3c. We observe that 5 iterations are enough for the maxima to stabilize. The increase in intensity of chosen output pixels through iterations is shown in Figure 3d. In Figure 3, approximately 23% of total intensity at 400 nm is focused to the designated spot and at 800 nm 10% of incident light is focused at the target. In fact, more than one-third of incident light is focused successfully to the desired positions.

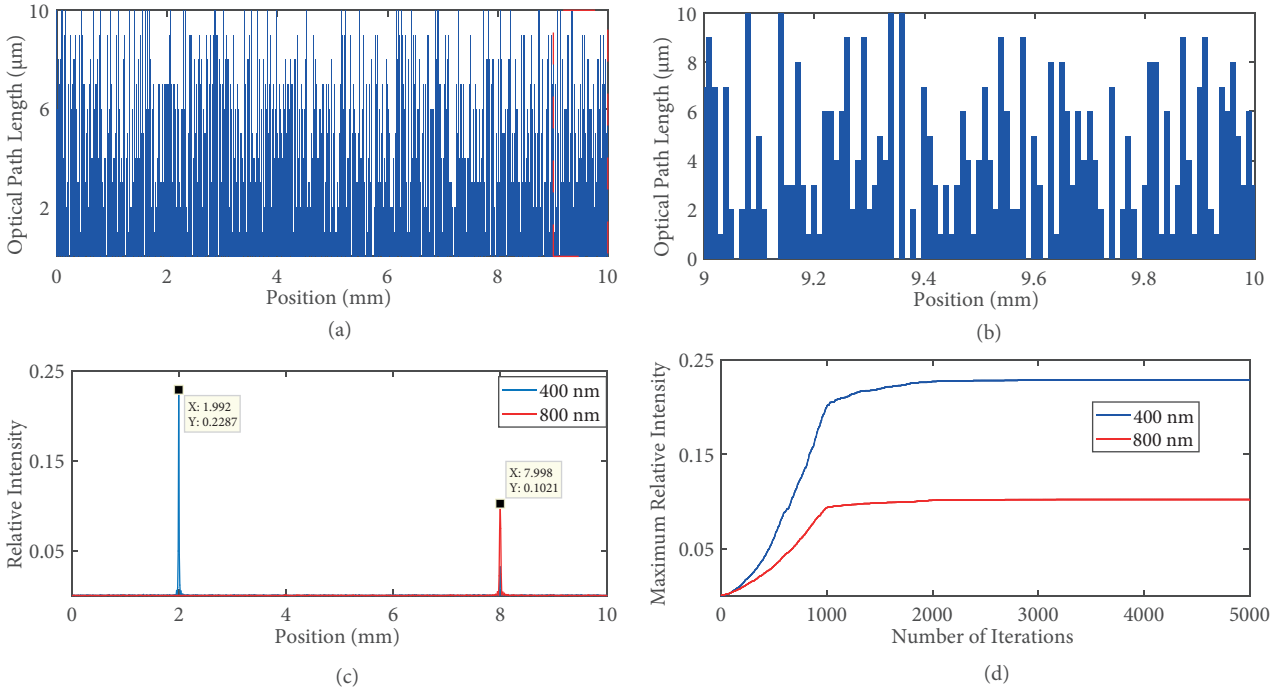

Figure 3. (a) Height profile of computationally calculated structure. (b) The high resolution view of the height profile between 9 and 10 mm. (c) Intensity distribution at output plane with a plane wave at the input plane. (d) Increase in maximum intensity versus number of iteration for our algorithm.

For two dimensions, the geometry is taken to be 10 mm $\times$ 10 mm and the target positions are chosen to be (2 mm, 8 mm) for 400 nm and (8 mm, 2 mm) for 800 nm. The resolution for the spectral splitter is 35 $\times$ 35 pixels. The calculation of G is performed using the relation presented in Eq. (4) for 2D holographic patterns. The resultant height profile is shown in Figure 4a and the resulting intensity pattern through the structure is shown in Figure 4b. The separation of two wavelengths is obvious and 36% of total intensity is accumulated at the desired pixels. For 400 nm, intensity of the selected pixel increases from 0.069% to 20%, while for 800 nm it increases from 0.207% to 16% after optimization. We also obtain results for different positions. In Figure 5, we set the target positions to (8 mm, 8 mm) for 400 nm and (2 mm, 2 mm) for 800 nm. The resulting height profile is shown in Figure 5a and the output intensity pattern is shown in Figure 5b. According to the results, this time 35% of total intensity (20% for 400 nm and 15% for 800 nm) is focused to the desired pixels. Figures 4 and 5 show that we can design the DOE and control the concentration of light for different wavelengths at desired positions.

4. Discussion

We would like to mention that in our algorithm the incoming light is considered to be coherent. It is well known that sunlight is partially coherent [11–14]. The partially coherent plane wave is spatially coherent within planes that are transverse to the propagation direction, while it is partially coherent in the axial direction. For finding the interference equation for two partially coherent beams, their normalized cross-correlation should be defined as [14]:

$$g_{12} = \frac{\langle U_1^* U_2 \rangle}{(I_1 I_2)^{1/2}} \tag{6}$$

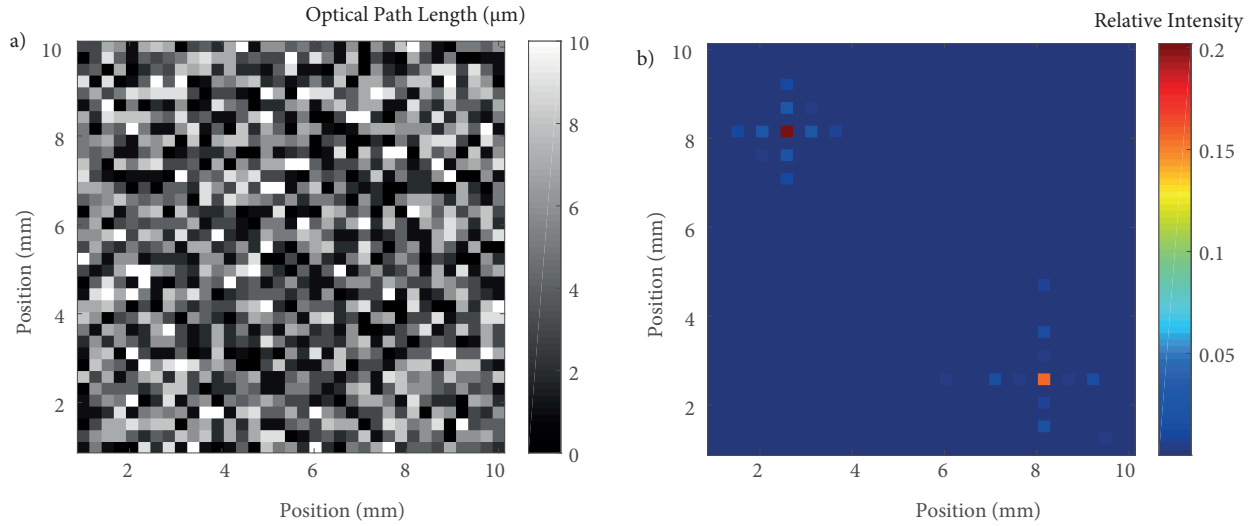

Figure 4. (a) Height profile of calculated 2D structure. (b) Intensity distribution at output plane with a plane wave input.

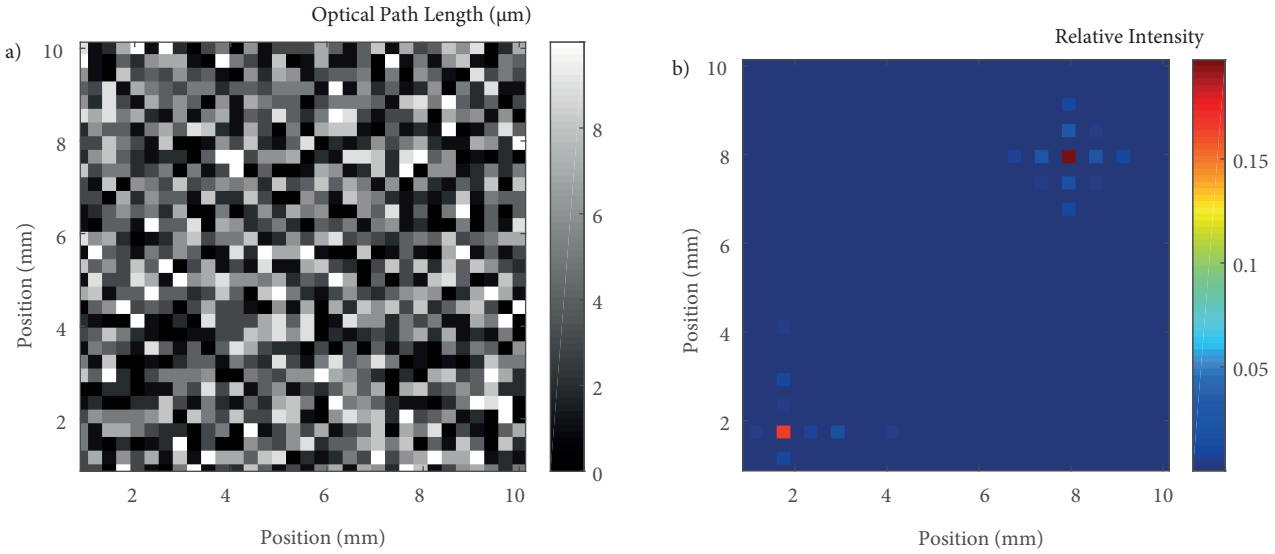

Figure 5. (a) Height profile of calculated 2D structure. (b) Intensity distribution at output plane with a plane wave input.

where U_1 and U_2 are two partially coherent waves with intensities I_1 and I_2. The resultant intensity of two interfering beams is:

$$I = \left\langle |U_1 + U_2|^2 \right\rangle = \left\langle |U_1|^2 \right\rangle + \left\langle |U_2|^2 \right\rangle + \langle U_1^* U_2 \rangle + \langle U_1 U_2^* \rangle \tag{7}$$

which can be written in terms of intensities as:

$$I = I_1 + I_2 + 2(I_1 I_2)^{1/2} |g_{12}| \, cos\varphi \tag{8}$$

where φ is the phase of g_{12}. In the case of two correlated beams, g_{12} becomes equal to $\exp(j\varphi)$. This leads to $|g_{12}| = 1$, so the equation evolves to an equation of interference of two beams with a phase difference φ. On the

other hand, for two uncorrelated beams, which leads to $|g_{12}| = 0$, the equation evolves to $I = I_1 + I_2$. This will result in no interference pattern, yet the intensities will be successfully summed up, which is desired for solar applications. For our approach, these two extreme cases are both acceptable since the first one is classical interference while the second one is the summing up of two intensities. If color holography were concerned, then the correlation would play a major role and would result in incorrect shapes for uncorrelated beams. However, we are interested in intensity for solar applications rather than the accuracy of the spatial shape.

For more generalized cases with a wider range of frequencies, the spectra of resultant intensity for incoherent and coherent cases are given by:

$$Incoherent: \quad F\{I_i\} = [H \times H]\,[G_g \times G_g]\,, \tag{9}$$

$$Coherent: \quad F\{I_i\} = HG_g \times HG_g \tag{10}$$

where $F\{I_i\}$ is the spectrum of resultant intensity, G_g is the spectrum of incoming light, and H is the amplitude transfer function [15]. The spatial profile of the interference pattern can be described using Eq. (9) and Eq. (10) for a broadband spectrum if accuracy is concerned rather than the total intensity at the target position.

5. Conclusion

The theoretical results show that more than 30% of light can be focused to designated positions, which can be set and optimized to fabrication criteria. Our designs offer increase in efficiency of solar cells given that the DOE acts simultaneously as a solar concentrator and as a spectral splitter, which are highly desired for multijunction solar cells. Increasing the number of pixels in the DOE or decreasing the step size in pixel values (resulting in increased number of steps within the same pixel height) results in more effective splitting. In both cases, the limiting factor is the calculation time, which increases drastically with the increase of number of pixels and number of steps. The calculation of a DOE that consists of 35 $\times$ 35 pixels with 11 height steps takes approximately 18 h, which can be further decreased using more advanced algorithms such as the genetic optimization method.

Acknowledgments

We would like to acknowledge METU project BAP-08-11-2016-066-2. We also would like to thank Alpan Bek, Raşit Turan, Bülent Akınoğlu, and Selçuk Bilmiş for useful discussions and facility support.

References

[1] Miller, O. D.; Yablonovitch, E.; Kurtz, S. R. *IEEE J. Photovolt.* **2012**, *3*, 1-27.

[2] Philipps, S. P.; Dimroth, F.; Bett A. W. In *McEvoy's Handbook of Photovoltaics: Fundamentals and Applications*; Di Ventra, M.; Evoy, S.; Heflin, J. R. Jr, Eds. Academic Press: London, UK, 2017, pp. 439-472.

[3] Kim, G.; Dominguez-Caballero, J. A.; Lee, H.; Friedman, D. J.; Menon, R. *Phys. Rev. Lett.* **2013,** *12*, 1-5.

[4] Gretzki, P.; Gillner, A. In *SPIE Proceedings Volume 10347, Optical Trapping and Optical Micromanipulation XIV: SPIE Nanoscience + Engineering, San Diego, CA, USA, 6–10 August 2017*; Dholakia, K.; Spalding, G. C., Eds.; The International Society for Optics and Photonics: Bellingham, WA, USA, 2017.

[5] Xie, H.; Ren, D.; Wang, C.; Mao, C.; Yang, L. *J. Mod. Opt.* **2018**, *65*, 255-261.

[6] Mohammad, N.; Meem, M.; Shen, B.; Wang, P.; Menon, R. *Sci. Rep.* **2018**, *8*, 2799.

[7] Gu, B. Y.; Yang, G. Z.; Dong, B. Z.; Chang, M. P.; Ersoy, O. K. *Appl. Opt.* **1995**, *14*, 2564-2570.

[8] Dong, B. Z.; Zhang, G. Q.; Yang, G. Z.; Gu, B. Y.; Zheng, S. H.; Li, D. H.; Chen, Y. S.; Cui, X. M.; Chen, M. L.; Liu, H. D. *Appl. Opt.* **1996**, *35*, 6859-6864.

[9] Yang, G.; Dong, B.; Gu, B.; Zhuang, J.; Ersoy, O. K. *Appl. Opt.* **1994**, *2*, 209-218.

[10] Vorndran, S.; Russo, J. M.; Wu, Y.; Pelaez, S. A.; Kostuk, R. K. *Opt. Express* **2015**, *24*, A1512-A1527.

[11] Agarwal, G. S.; Gbur, G.; Wolf, E. *Opt. Lett.* **2004**, *29*, 459-461.

[12] Mashaal, H.; Goldstein, A.; Feuermann, D.; Gordon, J. M. *Opt. Lett.* **2012**, *37*, 3516-3518.

[13] Divitt, S.; Novotny, L. *Optica* **2015**, *2*, 95-103.

[14] Saleh, B. E. A.; Teich, M. C. *Fundamentals of Photonics*, 1st ed.; John Wiley & Sons: New York, NY, USA, 1991.

[15] Goodman, J. W. *Introduction to Fourier Optics*, 3rd ed.; Roberts & Company Publishers: Englewood, CO, USA, 2005.